OXFORD JOURNAL
OF STUDENT
SCHOLARSHIP

The Age of the Universe: From Globular Clusters to Cosmological Parameters

Dhruv Punjabi
dpunjabi@jpischool.com

ABSTRACT

The age of the Universe is a fundamental cosmological parameter that can be inferred independently from stellar astrophysics and from theoretical cosmology, and comparing the two provides a stringent test of the ΛCDM model. Here we determine the absolute ages of seven Milky Way globular clusters from Hubble Space Telescope Advanced Camera for Surveys (ACS) photometry, and separately compute the age of the Universe by integrating the Friedmann equation with the Planck 2018 cosmological parameters. Cluster membership is established from the HUGS proper-motion catalogue, and the age, distance modulus, reddening, metallicity and $[\alpha/Fe]$ of each cluster are inferred jointly from the full colour-magnitude diagram using Dartmouth Stellar Evolution Database (DSED) isochrones within a Bayesian framework, following the likelihood of Valcin et al. (2020). The resulting ages range from 12.62 to 14.35 Gyr, with a statistical uncertainty of order 1 Gyr per cluster and a common systematic uncertainty of 0.5 Gyr from stellar modelling, consistent with previously published determinations for the same clusters. Given our considerably smaller sample than that of Valcin et al. (2020), we treat these ages as an independent, proof-of-concept check on the cosmological result rather than a population-level measurement. The Friedmann integral, evaluated with the Planck 2018 TT,TE,EE+lowE+lensing+BAO parameters with full propagation of their uncertainties, yields an age of the Universe of 13.792 ± 0.111 Gyr, in excellent agreement with the value tabulated directly by the Planck Collaboration for the same parameter combination, 13.787 ± 0.020 Gyr. The persistent tension between the CMB-inferred and distance-ladder-measured values of the Hubble constant is discussed as motivation for possible extensions to the standard model.

1. INTRODUCTION

The age of the Universe is a fundamental cosmological parameter, intricately linked to its expansion history and composition. Cosmologists determine this age by observing various cosmic phenomena and fitting them to theoretical models, primarily the Lambda Cold Dark Matter (ΛCDM) model (Verde et al. 2019). In this work we explore how the age of the Universe is derived from cosmological parameters, and we compare this determination to an independent one obtained from the colour-magnitude diagrams of Galactic globular clusters. The comparison of these two methods, one based in the physics of the early

Universe and one in the physics of stellar interiors, has long served as one of the more stringent consistency tests available to observational cosmology, and it is this comparison, updated with modern photometry and a modern Bayesian fitting method on the stellar side, that motivates the present work.

1.1 Determination from Cosmological Parameters

The expansion rate and the energy density of the Universe dictate its evolution and, consequently, its age. The Hubble parameter, defined as the fractional rate of change of the scale factor, describes the expansion rate as a function of time, while the energy density of the Universe influences this expansion. The Friedmann equation connects the Hubble parameter to the energy density and spatial curvature of the Universe (Ikape and Hlozek 2024).

The energy content of the Universe is typically divided into three components, each with a different equation-of-state parameter ω that governs how its energy density scales with the scale factor a (Ryden 2017).

- Radiation ($\omega = 1/3$): Energy density scales as a^{-4}. This component was dominant in the very early Universe.
- Matter ($\omega = 0$): Energy density scales as a^{-3}. This includes both baryonic matter, consisting of protons and neutrons, and cold dark matter. Matter dominated after the radiation-dominated era.
- Cosmological Constant or Dark Energy ($\omega = -1$): Energy density remains constant. This component drives the current accelerating expansion of the Universe.

The current density of each component, normalised to the critical density required for a spatially flat Universe, is represented by a density parameter. The standard ΛCDM model, which assumes a spatially flat Universe ($\Omega_k = 0$), uses six primary parameters, the baryon density $\Omega_b h^2$, the cold dark matter density $\Omega_c h^2$, the Hubble constant H_0, the scalar spectral index n_s, the reionisation optical depth τ, and the amplitude of the primordial power spectrum A_s. From these, other quantities, such as the total matter density $\Omega_m = \Omega_b + \Omega_c$ and the dark energy density Ω_Λ, can be derived (Planck Collaboration et al. 2020).

The age of the Universe is obtained by integrating the Friedmann equation from the Big Bang to the present, accounting for the contributions of all of these components. The benchmark model, adopted as the best fit to observational data, is spatially flat and contains radiation, matter and a cosmological constant. For this model, with Planck's best estimates for the parameters, the age of the Universe is close to 13.8 billion years.

1.2 Age Determination Methods

1.2.1 Cosmic Microwave Background

The Cosmic Microwave Background (CMB) is the residual heat from the Big Bang, and provides a snapshot of the Universe when it was approximately 380,000 years old (Knox 2019). At this epoch, commonly called recombination, the Universe had cooled to around 3000 K, sufficiently for electrons and protons to combine into neutral hydrogen, allowing photons to travel freely, forming the last scattering surface observed today as the CMB. The CMB exhibits small temperature fluctuations across the sky, at the level of about one part in 100,000, which record the density fluctuations of the early Universe that later seeded the formation of cosmic structure through gravitational instability.

CMB experiments, such as COBE, WMAP, and the Planck satellite, have measured these fluctuations with increasing precision (Knox 2019). The statistical properties of these temperature fluctuations are represented by the CMB power spectrum, whose shape and amplitude are sensitive to cosmological parameters including the density of matter and dark energy, and the curvature of space (Planck Collaboration et al. 2018). The location of the highest peak in the power spectrum, for example, is a strong indicator of the Universe's spatial curvature, consistent with a spatially flat Universe (Ryden 2017). By fitting the observed power spectrum to theoretical predictions, the Planck Collaboration has precisely constrained the ΛCDM parameters. We adopt throughout this work the parameters obtained from the combination of Planck temperature, polarisation, and lensing data (TT,TE,EE+lowE+lensing), supplemented in one instance by external Baryon Acoustic Oscillation (BAO) data (Planck Collaboration et al. 2020). The exact values used, and the reasoning behind this choice of data combination, are given in Section 2.2. These parameters, once inserted into the Friedmann equation, imply an age of the Universe close to 13.8 Gyr.

1.2.2 Globular Clusters

Globular clusters are ancient, compact, and, to good approximation, single-age stellar populations in the halo and bulge of the Milky Way, each comprising between 10^5 and 10^6 stars bound on eccentric orbits (Rowan and Coontz 2003). Their importance extends beyond stellar astrophysics into cosmology, since they provide a constraint on the age of the Universe that is independent of, and can be directly compared with, the value inferred from the CMB. Their low metal content indicates that they formed very early in the history of the Galaxy, so that their ages provide a robust lower limit on the age of the Milky Way, and hence of the Universe itself (Krauss and Chaboyer 2003).

The age of a globular cluster is most commonly obtained from the luminosity of its main-sequence turn-off point (MSTOP) in the colour-magnitude diagram (CMD). Because all stars in a cluster are coeval to good approximation, and differ from one another principally in mass, more massive stars evolve off the main sequence first, so the turn-off luminosity encodes the age of the population directly (Chaboyer 1994). Fitting the observed CMD with a theoretical isochrone, a curve computed from stellar evolution models for a fixed age, metallicity and helium abundance, allows the age of the cluster to be inferred from its turn-off. This isochrone-fitting technique, applied jointly to the full CMD rather than to the turn-off luminosity alone, is regarded as a well-established approach for determining precise cluster ages, distances and metallicities simultaneously (Valcin et al. 2020), and it is this full-diagram approach, described in Section 2.1, that we adopt here. Current determinations that use the full colour-magnitude diagram place the age of the oldest Galactic globular clusters at 13.3-13.8 Gyr, fully consistent with the CMB-inferred age of the Universe (Valcin et al. 2020, Krauss and Chaboyer 2003).

1.2.3 Comparison and Tensions

The agreement between the CMB-inferred age of the Universe and the ages of the oldest globular clusters is a cornerstone of the standard cosmological model. This consistency supports a Universe that is spatially flat, dark-energy dominated, and expanding at a rate described, to good approximation, by a single Hubble constant H_0.

A notable and persistent tension exists, however, concerning the value of H_0 itself. The CMB-inferred value from Planck is systematically lower than the value obtained from local, distance-ladder measurements based on Cepheids and Type Ia supernovae (Verde, Treu and Riess 2019). The most precise local determination, from Riess et al. (2019), gives $H_0 = (74.03 \pm 1.42)\ km\,s^{-1}\,Mpc^{-1}$, compared with the Planck value of $H_0 = (67.4 \pm 0.5)\ km\,s^{-1}\,Mpc^{-1}$. The discrepancy has grown from about 2.5 σ in 2013 to 4.4σ in 2019, despite extensive efforts to identify a systematic origin in either measurement, and other independent local probes, including strong lensing time delays, megamasers, and surface brightness fluctuations, likewise tend to prefer the higher local value.

This tension suggests that some aspect of the ΛCDM model may be incomplete. Simple extensions have not, so far, convincingly resolved it. Proposed solutions generally invoke new early-Universe physics, such as an early dark energy component or additional relativistic species, both of which would shrink the sound horizon and raise the CMB-inferred H_0 without degrading the otherwise excellent fit to the CMB power spectrum (Verde, Treu and Riess 2019).

2. METHODS

2.1 Age Determination Through Globular Clusters

2.1.1 Sample and Photometric Data

We determine the ages of seven Galactic globular clusters, M92, M22, M5, M15, NGC 6397, M13 and M4, chosen as a pilot sample of nearby, well-studied clusters spanning a range of metallicity, reddening and central concentration. Photometry for each cluster is drawn from the Hubble Space Telescope (HST) ACS Survey of Galactic Globular Clusters (GO-10775, PI: A. Sarajedini), which obtained deep imaging of sixty-five Galactic clusters through the F606W and F814W filters of the Wide Field Channel of the Advanced Camera for Surveys (Sarajedini et al. 2007). Each of the seven programme clusters was observed at a single epoch in 2006 (Anderson et al. 2008).

For every detected source, the released photometric catalogue reports pixel position, VEGAMAG magnitude and photometric error in each filter, right ascension and declination, and several quality diagnostics used below for membership and cleaning. Non-detections are excluded before further processing. The point-spread-function photometry is described by Anderson et al. (2008). Completeness, assessed via artificial-star tests, remains high across most of the field for the magnitude range used here and falls only in the innermost, most crowded regions of M15 and NGC 6397, the two most centrally concentrated clusters in our sample.

Instrumental magnitudes are placed on the VEGAMAG photometric system using the zero points of Sirianni et al. (2005), who also computed interstellar extinction coefficients for the ACS/WFC filters. For a G2-type spectral energy distribution, representative of an old, moderately metal-poor turn-off star, they find $R_{F606W} = 2.809$ and $R_{F814W} = 1.825$, as given in their Table 14. We adopt these values here as $A_X = R_X \cdot E(B - V)$ in the fitting likelihood of Section 2.1.5.

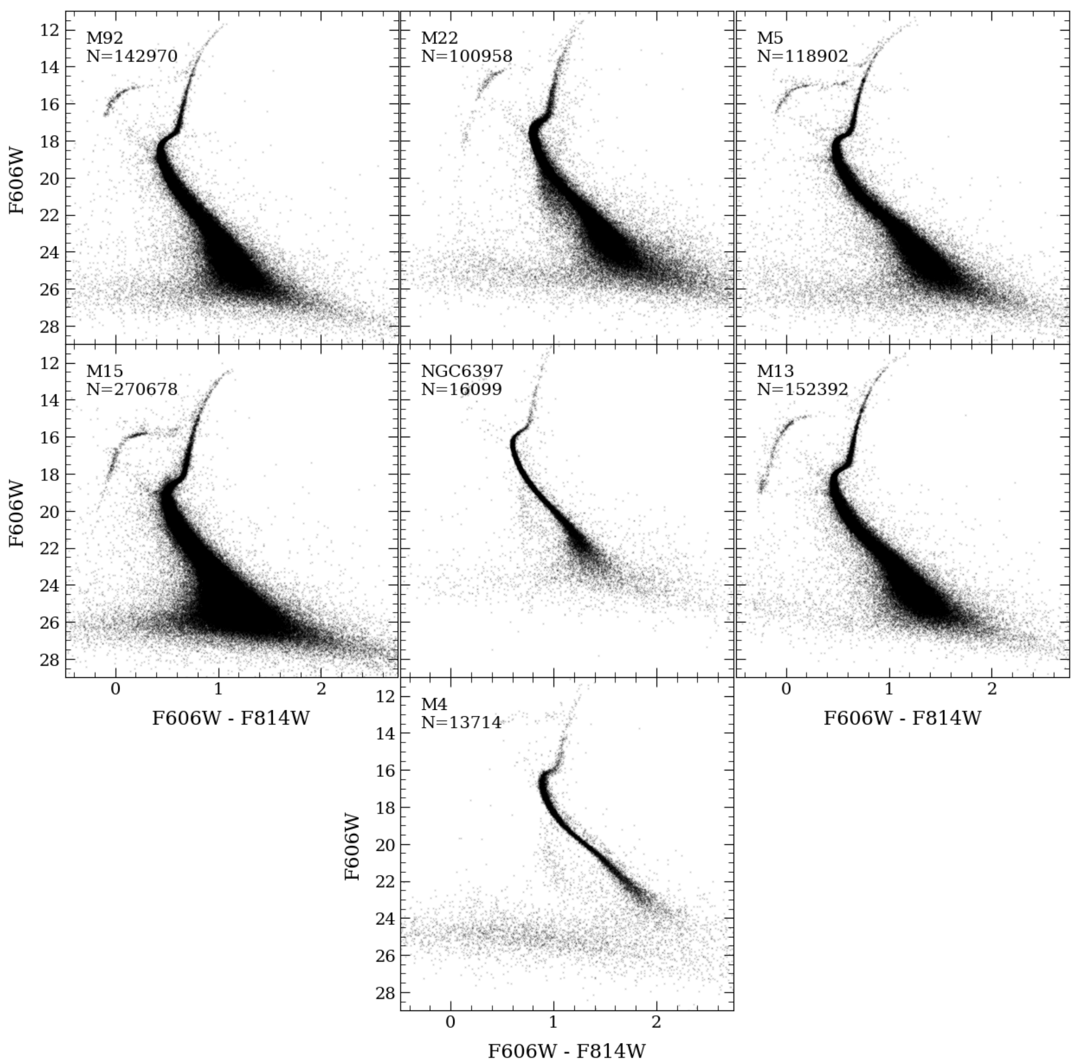

Figure 1: Raw colour-magnitude diagrams of the seven programme clusters prior to membership selection or differential-reddening correction, illustrating the field-star contamination and photometric scatter that the subsequent selection steps are designed to remove.

2.1.2 Cluster Membership

The ACS Survey Treasury photometry carries no proper-motion or membership information of its own. Kinematic membership is instead obtained by cross-matching the Treasury photometry against the HUGS catalogue (Hubble Space Telescope UV Globular Cluster Survey; Nardiello et al. 2018), which supplements a subset of the same clusters with additional multi-epoch imaging and reports internal, relative proper motions and membership probabilities computed with the software package KS2 (Bellini et al. 2017) via three independent photometric reductions. HUGS ties its own astrometry to the Gaia Data Release 1 reference frame at epoch 2015.0, giving a baseline of 8.7–9 years between the 2006 ACS epoch and the HUGS/Gaia tie for every cluster in our sample. This is long enough for internal cluster proper motions to be recovered as a signal (Nardiello et al. 2018).

For each star we cross-match against all three HUGS methods and retain whichever gives the closest astrometric match, first correcting for the cluster's mean proper motion and any residual frame-to-frame offset, solved from a subsample of bright, isolated stars, then matching positions to a tolerance of 0.1 arcsec. We adopt a membership-probability threshold of $P_{\mu} > 90\%$ on this best-matching method, since requiring confident detection in all three would discard many otherwise well-measured stars.

This membership criterion is necessarily incomplete toward the cluster centre, where crowding degrades the astrometry, and toward the faint main sequence, where proper-motion error becomes comparable to the internal velocity dispersion. Combined across all three HUGS methods, coverage is approximately 99% at F606W < 15, approximately 98% between F606W = 15–18, falls to 60–65% across the turn-off and subgiant branch (F606W = 18–20), and falls further, to 32–43%, on the faint main sequence (F606W = 20–26). We regard this as an acceptable, quantified limitation rather than a hidden one, since the likelihood of Section 2.1.5 draws most of its age information from the turn-off and subgiant branch, where coverage remains highest.

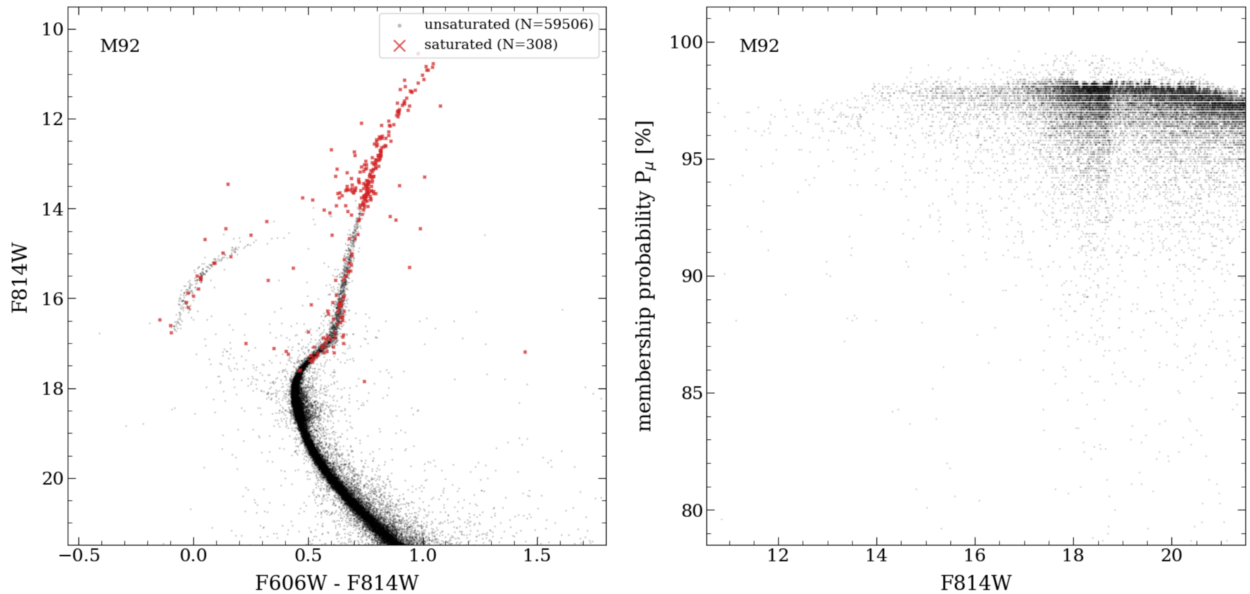

Figure 2: Colour-magnitude diagram with saturated stars flagged (left) and membership probability as a function of F814W magnitude (right) for a representative programme cluster.

2.1.3 Photometric Quality Cuts

We apply the same photometric quality prescriptions used by Wagner-Kaiser et al. (2017) for the identical ACS Survey photometry, also followed by Valcin et al. (2020). Stars whose photometric error, in both filters, falls in the outer 5% tail for that cluster are removed, as are stars whose frame-to-frame positional discrepancy, in either filter, falls in the outer 2.5% tail. The latter cut is skipped for NGC 6397, whose brighter stars were observed only in short exposures. No statistical field-star decontamination is applied, since the ACS/WFC field of view, approximately 3.4×3.4 arcmin, lies within the tidal radius of essentially every cluster in our sample, leaving no external field region from which to build a comparison Hess diagram. Field contamination is instead handled entirely by the kinematic membership selection above.

2.1.4 Colour-Magnitude Diagram Construction and Differential Reddening Correction

For each cluster we construct the observed colour-magnitude diagram in F606W versus F606W − F814W, matching the convention of Valcin et al. (2020). We retain apparent, rather than absolute, magnitudes, since the distance modulus is treated as a free parameter in the fit of Section 2.1.5, avoiding the circularity that would otherwise arise from adopting a fixed distance. The magnitude range used in the fit extends from the brightest unsaturated stars down to F606W = 26, following Valcin et al. (2020).

Two clusters in our sample, M4 and M22, lie behind a patchy foreground dust distribution that produces measurable differential reddening across their fields (Hendricks et al. 2012, Marino et al. 2011). Left uncorrected, this broadens the observed main sequence and subgiant branch and can bias the joint fit of

Section 2.1.5. Legnardi et al. (2023), who surveyed differential reddening across fifty-six ACS Survey clusters, quantify the reddening variation using the 68th-percentile amplitude of the differential-reddening distribution in F814W, $\sigma_A(F814W)$. Table 1 gives their measured amplitude for each of our seven programme clusters. Only M22 and M4 exceed the amplitude at which a correction is warranted.

Table 1: Differential-reddening amplitude for the seven programme clusters (Legnardi et al. 2023). Only M22 and M4 exceed the amplitude at which a correction is warranted.

Cluster	**NGC**	$\sigma_A(F814W)$ **(mag)**	**Correction applied**
M92	6341	0.007	No
M22	6656	0.012	Yes
M5	5904	0.005	No
M15	7078	0.008	No
NGC 6397	6397	0.007	No
M13	6205	0.006	No
M4	6121	0.020	Yes

We correct M4 and M22 following the local, star-by-star method of Ying et al. (2024), itself a development of the local-neighbour approach described by Milone et al. (2012). A fiducial ridgeline is fitted through the cluster's main sequence, and the colour-magnitude diagram is rotated about a point near the subgiant branch by an angle

$$\theta = arctan\left[\frac{A_{F606W}}{A_{F606W} - A_{F814W}}\right]$$

where A_{F606W} and A_{F814W} are extinction coefficients appropriate to a cool $T_{eff} \approx 4000$ K star, interpolated from the grid of Bedin et al. (2005) at the cluster's Harris (1996, 2010 edition) $E(B - V)$. For each star, the perpendicular offset from the rotated fiducial is measured for its 50 nearest spatial neighbours, and the median of these offsets, chosen over the mean to avoid biasing the correction toward the photometric binary sequence (Ying et al. 2024), is subtracted before rotating back to the original system. The five remaining clusters, whose reddening amplitude falls below the Legnardi et al. (2023) threshold, receive no colour correction.

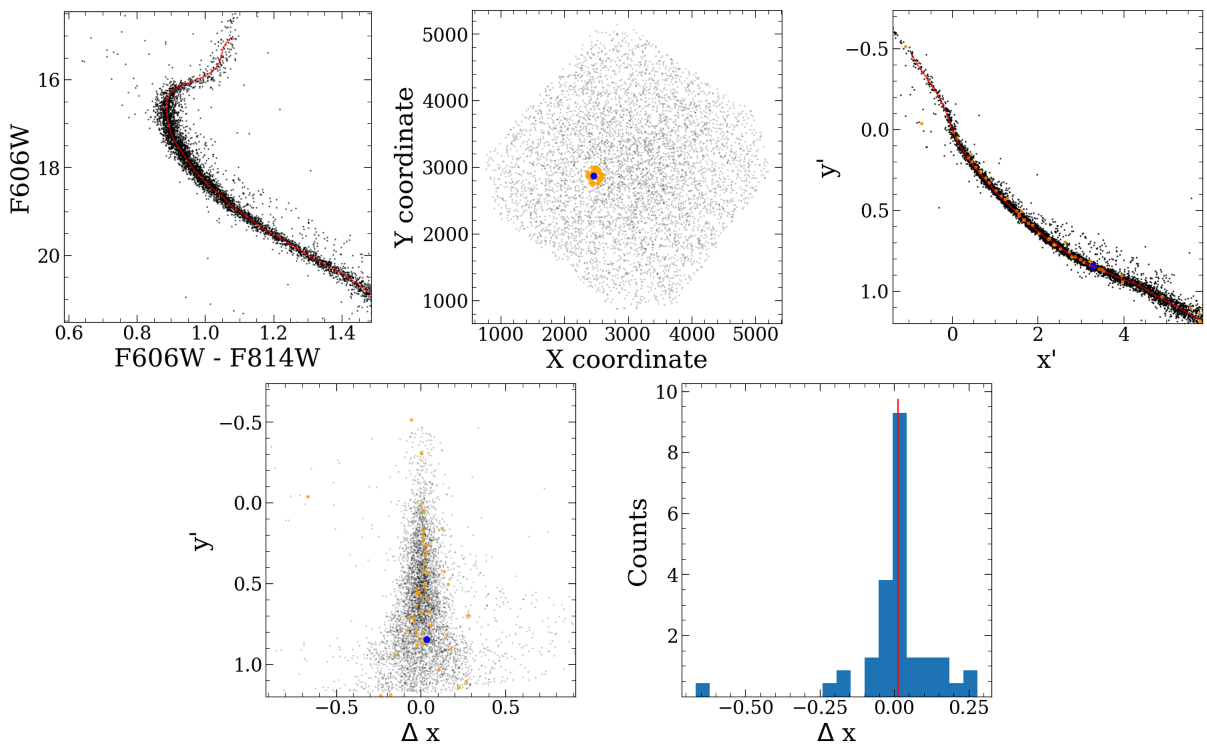

Figure 3: Illustration of the differential-reddening correction procedure for a representative reddened cluster in our sample: the fiducial ridgeline (a), the target star and its 50 nearest spatial neighbours (b), the rotated colour-magnitude diagram with rotated fiducial (c), the neighbours' offsets from the fiducial (d), and the resulting distribution of offsets with the adopted median indicated (e).

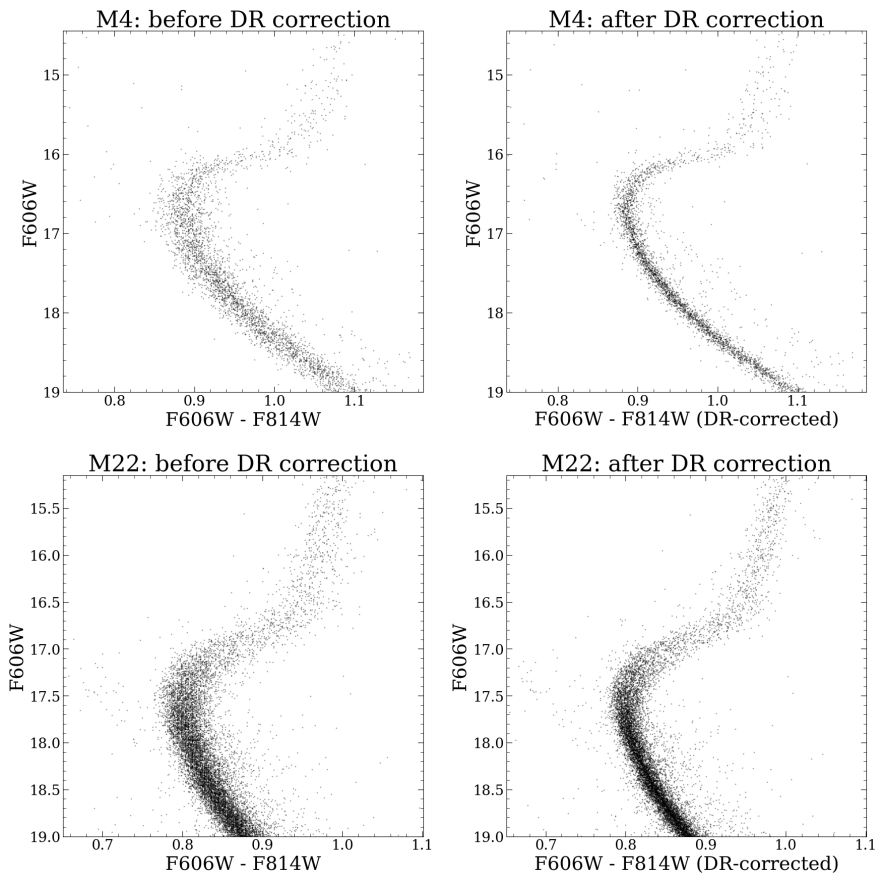

Figure 4: Colour-magnitude diagrams of M4 and M22 before and after the differential-reddening correction described in the text, illustrating the resulting narrowing of the main sequence and subgiant branch.

2.1.5 Isochrones and Bayesian Parameter Inference

Theoretical isochrones are drawn from the Dartmouth Stellar Evolution Database (DSED, Dotter et al. 2008), a grid of stellar evolution models spanning the age, metallicity, $[\alpha/Fe]$ and helium-abundance range appropriate to Galactic globular clusters, transformed to the ACS/WFC filter system. Metallicity and $[\alpha/Fe]$ are interpolated continuously within this grid, with nodes spaced at 0.2 dex in $[\alpha/Fe]$, from −0.2 to +0.8. $[\alpha/Fe]$ is the parameter most responsible for breaking the age–metallicity degeneracy, since its effect on the main-sequence colour is small near the turn-off but grows toward fainter magnitudes (Dotter et al. 2008), allowing it to be constrained jointly with age and metallicity from the full colour-magnitude diagram.

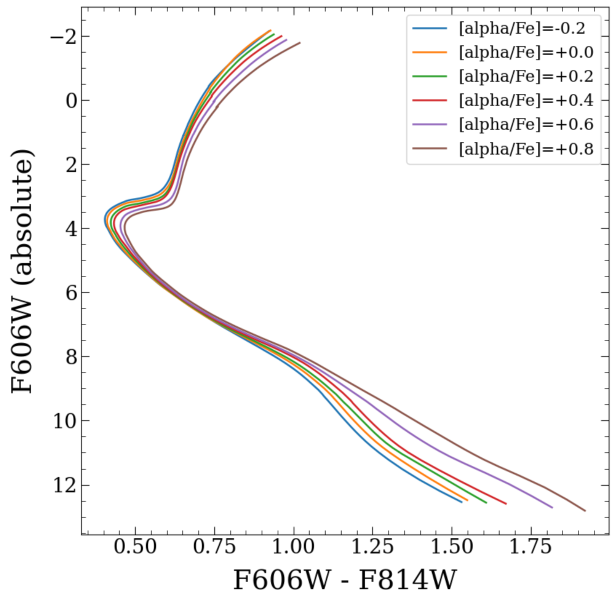

Figure 5: Dependence of the DSED main-sequence colour on [α/Fe] at fixed age and metallicity, illustrating how the effect grows from the turn-off toward fainter magnitudes.

We follow closely the Bayesian inference method of Valcin et al. (2020), in which the age, distance modulus, reddening, $[Fe/H]$ and $[\alpha/Fe]$ of each cluster are inferred jointly from the full colour-magnitude diagram rather than from the turn-off luminosity alone. The additional information in the main sequence below the turn-off and the subgiant/lower-red-giant branch above it substantially reduces the age–distance–metallicity degeneracy that limits a turn-off-only analysis. This differs from the approach of Dotter et al. (2010) for the same cluster sample, who match isochrones to the turn-off and horizontal-branch magnitudes alone.

Stars brighter than the model turn-off that deviate by more than 0.15 mag from a reference isochrone's horizontal-branch/asymptotic-giant-branch locus are removed before fitting, since the DSED models used here do not include these evolutionary phases. Following Valcin et al. (2020), each cluster's CMD is split, at the model's own turn-off, recomputed at every MCMC step, into a main-sequence region and an upper-branch (subgiant/lower-RGB) region, each independently binned in magnitude, with 0.2 mag bins and main-sequence bins retained only with at least five member stars. Within each bin the median observed colour is compared with the isochrone-predicted colour, with the log-likelihood

$$lnL = -\frac{1}{2}\sum\frac{\left(C_i^{data}-C_i^{th}\right)^2}{\sigma_i^2}$$

summed separately over the two regions. Bin uncertainties are estimated from the star-to-star colour scatter within the bin via the standard error of the median, and bins containing fewer than eight stars, or whose colour distribution fails a test for unimodality, a sign of contamination or an unrecognised sub-population, are dropped, following the quality-control procedure of Valcin et al. (2020, Appendix C).

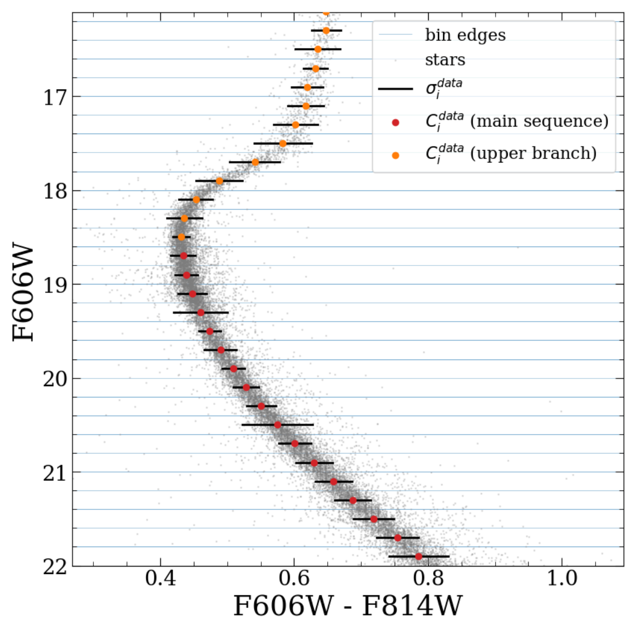

Figure 6: Split of a representative programme cluster's colour-magnitude diagram into main-sequence and upper-branch regions, with the adopted magnitude bins and the resulting median colour points overlaid.

The five free parameters, age, distance modulus, $E(B - V)$, $[Fe/H]$ and $[\alpha/Fe]$, are sampled with the affine-invariant MCMC ensemble sampler of Foreman-Mackey et al. (2013), under Gaussian priors on distance modulus, metallicity, reddening and $[\alpha/Fe]$ centred on independent literature values, and a flat prior on age over the DSED grid's full range, 1–15 Gyr. For six clusters these priors are centred on the values tabulated by Dotter et al. (2010). M22, excluded from that table owing to a known double subgiant branch indicative of multiple stellar populations, instead uses the Harris (1996, 2010 edition) metallicity and reddening, the distance of Baumgardt and Vasiliev (2021), and the $[\alpha/Fe]$ of Pritzl et al. (2005). M4's reddening prior is centred on the RR Lyrae-based value of Hendricks et al. (2012), following Valcin et al. (2020)'s own substitution for this cluster. Reddening is bounded to be non-negative, metallicity is truncated at the DSED grid's low-metallicity edge, and helium abundance is held fixed at $Y \approx 0.245 - 0.25$.

Table 2 gives the complete set of Gaussian prior centres adopted for each cluster and parameter. Prior widths are common to all clusters, $\sigma = 0.2$ dex $[Fe/H]$, $\sigma = 0.5$ mag distance modulus, $\sigma = 0.02$ mag $E(B - V)$, and $\sigma = 0.2$ dex $[\alpha/Fe]$.

Table 2: Gaussian prior centres adopted for each fitted parameter, with age omitted because it is given a flat prior.

Cluster	$[Fe/H]$ **centre**	$(m - M)_0$ **centre**	$E(B - V)$ **centre**	$[\alpha/Fe]$ **centre**	**Source**
M92	-2.40	14.7635	0.02	0.2	Dotter (2010)
M22	-1.70	12.595	0.34	0.4	Harris/BV21/Pritzl
M5	-1.30	14.3253	0.03	0.2	Dotter (2010)
M15	-2.40	15.2175	0.10	0.2	Dotter (2010)
NGC 6397	-2.10	12.0715	0.18	0.2	Dotter (2010)
M13	-1.60	14.4335	0.02	0.2	Dotter (2010)
M4	-1.20	11.5248	0.37	0.4	Dotter (2010)/ Hendricks (2012)

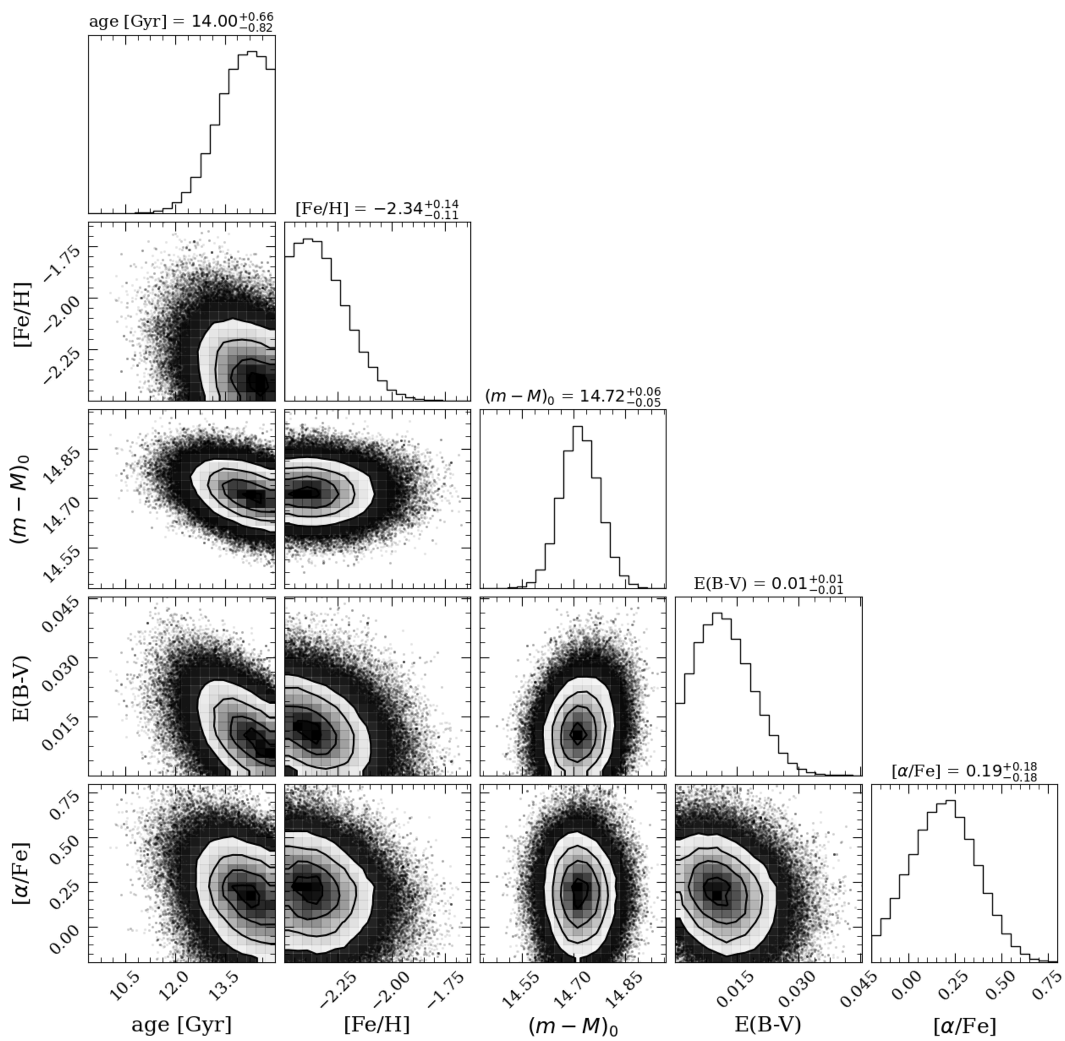

Figure 7: Marginalised one- and two-dimensional posterior distributions, age, $[Fe/H]$, distance modulus, $E(B - V)$, $[\alpha/Fe]$, for M92, a representative cluster, illustrating the degeneracies among the fitted parameters and their comparison with the adopted priors.

2.1.6 MCMC Sampling and Convergence

Each cluster is fitted with an ensemble of one hundred walkers run for five thousand steps, the first five hundred discarded as burn-in, using a fixed random seed. We inspect the trace of each parameter to check convergence and identify walkers trapped in non-physical regions of parameter space, a known failure mode arising from the age–distance–metallicity degeneracy near the old-age, low-metallicity extreme of the grid (Valcin et al. 2020). Walkers whose post-burn-in mean lies more than five median absolute deviations from the ensemble median are excluded and credible intervals recomputed from the cleaned sample. Between zero and three of the one hundred walkers are excluded per cluster, and every retained ensemble has an acceptance fraction between 0.48 and 0.52, within the healthy range for this sampler (Foreman-Mackey et al. 2013).

2.1.7 Systematic Uncertainties

Following Valcin et al. (2020), we report a statistical uncertainty on each cluster's age from the 68% highest-posterior-density interval of its marginalised posterior, together with a common systematic uncertainty of 0.5 Gyr arising from the stellar models themselves. This comprises 0.3 Gyr from the uncertain mixing-length parameter, calibrated to the Sun rather than measured directly for metal-poor cluster stars, and 0.2 Gyr from nuclear reaction rates and radiative opacities used in the stellar evolution calculations. These are added linearly, as in Valcin et al. (2020), since both are one-directional systematics in the same underlying stellar model rather than independent random errors. This systematic is identical for every cluster, since all seven are fitted with the same DSED grid.

2.2 Friedmann Equations and Cosmological Parameters

2.2.1 Foundation

The standard model of the Universe's evolution is built upon the Friedmann-Lemaître-Robertson-Walker (FLRW) metric, which describes a spacetime that is spatially homogeneous and isotropic (Kumar 2013), a cosmological principle supported by, among other observations, the near-uniformity of the CMB itself (Zee 2013). Written in comoving spherical coordinates (r, θ, ϕ), the line element of this metric is

$$ds^2 = - c^2 dt^2 + a^2(t)\frac{dr^2}{1-kr^2} + a^2(t)r^2\left(d\theta^2 + sin^2\theta\, d\phi^2\right)$$

where the scale factor $a(t)$ carries the entire dynamical content of the model, and is conventionally normalised so that its present-day value is $a = 1$. The scale factor is related to the redshift z of an observed source by

$$a(t) = \frac{1}{1+z}$$

so that larger redshift corresponds to earlier cosmic time, when the scale factor was smaller (Zee 2013).

2.2.2 Curvature and Spatial Geometry

The spatial geometry of the FLRW spacetime is set by a curvature parameter k, which may take the values $+1$, 0 or -1, corresponding respectively to a closed, flat or open Universe. In a flat Universe ($k = 0$), the spatial geometry is Euclidean and the total density equals the critical density, $\Omega_{total} = 1$. Current observations, in particular the combination of Planck CMB data with Baryon Acoustic Oscillation measurements, indicate that the Universe is consistent with spatial flatness to within 0.2% (Planck Collaboration et al. 2020). A closed Universe ($k = +1$, $\Omega_{total} > 1$) will eventually recollapse in a Big Crunch, while an open Universe ($k = -1$, $\Omega_{total} < 1$) expands forever.

2.2.3 Friedmann Equations and Dynamics

The evolution of the scale factor is governed by two coupled, non-linear differential equations derived by Alexander Friedmann from Einstein's field equations (Uzan and Lehoucq 2001). The Hubble parameter, defined as the fractional rate of change of the scale factor,

$$H(t) = \frac{\dot{a}(t)}{a(t)}$$

takes, at the present epoch, the value of the Hubble constant, H_0. The first Friedmann equation relates the square of the Hubble parameter to the energy density ρ, the curvature, and the cosmological constant Λ,

$$H^2(t) = \frac{8\pi G}{3}\rho(t) - \frac{kc^2}{a^2(t)} + \frac{\Lambda c^2}{3}$$

and is the general-relativistic analogue of the energy-conservation equation (Uzan and Lehoucq 2001). The second Friedmann equation governs the acceleration of the expansion,

$$\frac{\ddot{a}(t)}{a(t)} = -\frac{4\pi G}{3}\left(\rho(t) + \frac{3p(t)}{c^2}\right)$$

and the two equations are related by the continuity equation, expressing conservation of the stress-energy tensor for a perfect fluid,

$$\frac{d\rho}{dt} + 3\frac{\dot{a}(t)}{a(t)}\left(\rho(t) + \frac{p(t)}{c^2}\right) = 0$$

2.2.4 Cosmological Parameters

The contents of the Universe are characterised by the equation of state relating pressure and energy density,

$$p(t) = \omega c^2 \rho(t)$$

where ω is the dimensionless equation-of-state parameter (Nemiroff and Patla 2007), and the energy density of a component with equation of state ω scales with the scale factor as

$$\rho \propto a^{-3(1+\omega)}$$

The critical density, the density required for spatial flatness, is

$$\rho_c = \frac{3H_0^2}{8\pi G}$$

and the density parameters used throughout this work are defined as the ratio of each component's present-day density to the critical density,

$$\Omega = \frac{\rho(t)}{\rho_c} = \frac{8\pi G \rho(t)}{3H_0^2}$$

so that the first Friedmann equation, evaluated at the present epoch, requires $\Omega_{total} + \Omega_k = 1$, with $\Omega_{total} = \Omega_m + \Omega_r + \Omega_\Lambda$.

2.2.5 The Planck 2018 Measurement

The parameters used in this section are inferred by fitting the FLRW model to the angular power spectrum of the CMB temperature and polarisation anisotropies observed by Planck. The acoustic-peak scale, set by the sound horizon at recombination and the angular-diameter distance to the last-scattering surface, is the dominant constraint on Ω_m, Ω_Λ and H_0. The relative heights of successive peaks separately constrain the baryon and cold-dark-matter densities, while large-scale polarisation constrains the reionisation optical depth. Planck's measurement of the CMB lensing power spectrum provides an additional, partially independent constraint on Ω_m, and is included in every parameter combination used here. We adopt the combination that also includes external BAO distance measurements, for the reason given in Section 2.2.8.

2.2.6 The Friedmann Integral

Rewriting the first Friedmann equation in terms of the scale factor, the age of the Universe t_0 is obtained by integrating

$$dt = \frac{da}{aE(a)}$$

from the Big Bang ($a = 0$) to the present ($a = 1$), where

$$E(a) = \sqrt{\Omega_{r,0}a^{-4} + \Omega_{m,0}a^{-3} + \Omega_{k,0}a^{-2} + \Omega_{\Lambda}}$$

so that

$$t_0 = \frac{1}{H_0}\int_0^1 \frac{da}{aE(a)}$$

Substituting $a = \frac{1}{(1+z)}$, an equivalent and numerically more convenient form is

$$t_0 = \frac{1}{H_0}\int_0^{z_{max}} \frac{dz}{(1+z)E(z)}$$

Physically, $\frac{1}{E(a)}$ measures the instantaneous expansion rate relative to H_0. Since matter and radiation redshift more steeply than dark energy as a shrinks, $E(a)$ grows without bound as $a \to 0$, and it is only because the integrand $\frac{1}{[aE(a)]}$ falls off fast enough that the age of the Universe is finite at all.

2.2.7 Parameter Values and Worked Substitution

Step 1: H_0 **and** Ω_m

Planck 2018 VI, Table 2, column "TT,TE,EE+lowE+lensing+BAO" (Planck Collaboration et al. 2020):

$$H_0 = 67.66 \pm 0.42\ km\,s^{-1}\,Mpc^{-1}$$
$$\Omega_{m,0} = 0.3111 \pm 0.0056$$

Step 2: Ω_k

Planck 2018 VI, Eq. 47b, the curvature-extension fit to the identical data combination:

$$\Omega_{k,0} = 0.0007 \pm 0.0019$$

Step 3: Ω_r

Planck fixes the present-day CMB temperature to $T_0 = 2.7255 \pm 0.0006$ K (Fixsen 2009) and holds the effective number of relativistic species at the Standard Model value $N_{eff} = 3.046$. The photon density follows from the Stefan-Boltzmann law,

$$\Omega_{\gamma,0}h^2 = 2.4728 \times 10^{-5}$$

Scaling up for neutrinos via

$$\Omega_{r,0}h^2 = \Omega_{\gamma,0}h^2\left[1 + \frac{7}{8}\left(\frac{4}{11}\right)^{4/3}N_{eff}\right]$$

the bracketed factor evaluates to 1.6918, giving

$$\Omega_{r,0}h^2 = 4.1834 \times 10^{-5}$$

Dividing by $h^2 = 0.6766^2 = 0.45778$,

$$\Omega_{r,0} = \frac{4.1834\times10^{-5}}{0.45778} = 9.14 \times 10^{-5}$$

This is negligible next to the other terms and is held fixed at this value throughout.

Step 4: Ω_Λ

The relation:

$$\Omega_m + \Omega_\Lambda + \Omega_r + \Omega_k = 1$$

must hold for any single, internally consistent parameter set. Table 2's own tabulated $\Omega_\Lambda = 0.6889$ was fit assuming $\Omega_k \equiv 0$ exactly, the flat base model. Substituting it together with the non-zero Ω_k from Step 2 overshoots unity by 0.079%, an inconsistency from combining two different Planck fits. We therefore re-derive Ω_Λ from closure instead:

$$\Omega_\Lambda = 1 - \Omega_m - \Omega_r - \Omega_k$$
$$= 1 - 0.3111 - 0.0000914 - 0.0007 = 0.688109$$

As a check, substituting all four values at $z = 0$, $a = 1$, gives

$$E(0) = \sqrt{0.0000914 + 0.3111 + 0.0007 + 0.688109} = 1.0000$$

exactly, as required since $H(0) = H_0$ by definition.

Step 5: integrate

Equation (15) is evaluated numerically using adaptive quadrature from $z = 0$ to $z_{max} = 10^5$. The result changes by less than 10^{-6} Gyr as z_{max} is varied between 10^4 and 10^6, confirming that the tail beyond last scattering, $z \approx 1100$, contributes negligibly. Carrying out this integration with the Step 1-4 values gives

$$t_0 = 13.792\, Gyr$$

using 1 Mpc = 3.086×10^{22} m and 1 Gyr = 3.154×10^{16} s to convert the integral's natural units of H_0^{-1} into Gyr.

2.2.8 Why the BAO Combination

Planck's own paper states its overall baseline as "TT,TE,EE+lowE+lensing", with no BAO. We use the +BAO combination instead because it provides a consistent basis for incorporating the measured curvature parameter Ω_k. The curvature-extension fit to the no-BAO baseline gives $\Omega_k = -0.0106 \pm 0.0065$, a $\sim 1.6\sigma$ departure from flatness, reflecting a geometric degeneracy in CMB-alone analyses that Planck's own text states is only decisively broken by adding BAO, Sect. 7.3. Since Step 2 above uses a measured Ω_k rather than assuming flatness, the internally consistent choice is the data combination for which that measured curvature is small and consistent with zero, namely +BAO.

2.2.9 Uncertainty Propagation

H_0, Ω_m and Ω_k are propagated via Monte Carlo, using 500,000 samples and independent Gaussians centred on the Step 1-2 values with their quoted 1σ widths. Independence is a documented simplifying assumption, since Planck does not publish a correlation matrix for these parameters in its paper text. Ω_Λ is recomputed for every sample from the Step 4 closure relation rather than sampled independently, and the full non-linear integral, Eq. 14, is evaluated exactly for each sample, giving a mean age of 13.7933 Gyr. An independent linear, delta-method cross-check, holding the closure relation fixed, gives a quadrature-summed uncertainty of 0.1107 Gyr, agreeing with the Monte Carlo result to three significant figures. Combining the two methods,

$$t_0 = 13.792 \pm 0.111\, Gyr$$

This uncertainty is somewhat larger than the value quoted directly by the Planck Collaboration for the same parameter combination, 13.787 $\pm$ 0.020 Gyr, because our propagation treats H_0, Ω_m and Ω_k as statistically independent, whereas the Planck posterior chains contain a well-known anti-correlation between H_0 and Ω_m that partially cancels in the age integral and is not recoverable from the summary statistics published in Table 2 of Planck Collaboration et al. (2020). Our quoted uncertainty should accordingly be understood as a conservative upper bound.

3. RESULTS

3.1 Globular Cluster Age Determination

Table 3 reports the marginalised posterior median and 68% credible interval for the age, metallicity, distance modulus, reddening and $[\alpha/Fe]$ of each of the seven programme clusters, together with the common 0.5 Gyr systematic uncertainty of Section 2.1.7. The resulting ages range from 12.62 Gyr, M5, to 14.35 Gyr, NGC 6397, with a typical statistical uncertainty of order 1 Gyr per cluster. Every cluster is consistent, at the combined statistical and systematic level, with the CMB-inferred age of the Universe derived in Section 3.2.

Table 3: Marginalised posterior median and 68% credible interval for each fitted parameter of the seven programme clusters. Ages are quoted with the statistical uncertainty from the MCMC posterior followed by the common systematic uncertainty of 0.5 Gyr.

Cluster	Age (Gyr)	$[Fe/H]$	Distance Modulus	$E(B-V)$	$[\alpha/Fe]$
M92	$13.99^{+0.66}_{-0.82} \pm 0.5$	$-2.34^{+0.14}_{-0.11}$	$14.72^{+0.06}_{-0.05}$	$0.011^{+0.007}_{-0.006}$	$0.19^{+0.18}_{-0.18}$
M22	$14.03^{+0.68}_{-1.07} \pm 0.5$	$-1.73^{+0.15}_{-0.15}$	$12.68^{+0.06}_{-0.06}$	$0.347^{+0.009}_{-0.010}$	$0.38^{+0.18}_{-0.18}$
M5	$12.62^{+1.22}_{-1.24} \pm 0.5$	$-1.31^{+0.15}_{-0.16}$	$14.35^{+0.06}_{-0.06}$	$0.024^{+0.011}_{-0.011}$	$0.20^{+0.18}_{-0.17}$
M15	$13.63^{+0.89}_{-1.10} \pm 0.5$	$-2.34^{+0.15}_{-0.11}$	$15.21^{+0.08}_{-0.08}$	$0.077^{+0.010}_{-0.010}$	$0.18^{+0.18}_{-0.19}$
NGC 6397	$14.35^{+0.46}_{-0.74} \pm 0.5$	$-2.08^{+0.19}_{-0.17}$	$12.04^{+0.04}_{-0.04}$	$0.169^{+0.008}_{-0.008}$	$0.25^{+0.19}_{-0.20}$
M13	$13.45^{+0.94}_{-1.17} \pm 0.5$	$-1.63^{+0.16}_{-0.15}$	$14.47^{+0.06}_{-0.06}$	$0.010^{+0.008}_{-0.006}$	$0.20^{+0.17}_{-0.18}$
M4	$13.50^{+1.00}_{-1.27} \pm 0.5$	$-1.15^{+0.14}_{-0.15}$	$11.44^{+0.05}_{-0.05}$	$0.404^{+0.010}_{-0.009}$	$0.41^{+0.16}_{-0.15}$

Table 4 compares our seven ages against three published sets. Valcin et al. (2020) provide the most direct comparison, since their likelihood, priors and quality-control procedure are followed throughout Section 2.1.5, and report all seven clusters. VandenBerg et al. (2013) fit the turn-off and horizontal-branch magnitudes of largely independent photometry with their own stellar models, reporting all seven. Dotter et al. (2010) fit only the turn-off and horizontal-branch magnitudes of the same ACS Survey photometry with the same DSED models, reporting six of our seven, excluding M22 for the reason given in Section 2.1.5.

Table 4: Direct comparison of the ages derived in this work with previously published values for the same clusters.

Cluster	This work (Gyr)	Valcin et al. (2020) (Gyr)	VandenBerg et al. (2013) (Gyr)	Dotter et al. (2010) (Gyr)
M92	$13.99^{+0.66}_{-0.82} \pm 0.5$	$13.30^{+0.60}_{-0.60} \pm 0.5$	12.75 ± 0.25	13.25 ± 1.00
M22	$14.03^{+0.68}_{-1.07} \pm 0.5$	$14.54^{+0.36}_{-0.97} \pm 0.5$	12.50 ± 0.50	Not reported
M5	$12.62^{+1.22}_{-1.24} \pm 0.5$	$12.75^{+0.80}_{-0.80} \pm 0.5$	11.50 ± 0.25	12.25 ± 0.75
M15	$13.63^{+0.89}_{-1.10} \pm 0.5$	$13.28^{+0.82}_{-0.71} \pm 0.5$	12.75 ± 0.25	13.25 ± 1.00
NGC 6397	$14.35^{+0.46}_{-0.74} \pm 0.5$	$14.21^{+0.69}_{-0.69} \pm 0.5$	13.00 ± 0.25	13.50 ± 0.50
M13	$13.45^{+0.94}_{-1.17} \pm 0.5$	$13.49^{+0.62}_{-0.45} \pm 0.5$	12.00 ± 0.38	13.00 ± 0.50
M4	$13.50^{+1.00}_{-1.27} \pm 0.5$	$13.01^{+1.01}_{-1.01} \pm 0.5$	11.50 ± 0.38	12.50 ± 0.50

Our ages agree with Valcin et al. (2020) within their own quoted uncertainty for six of the seven clusters. For the seventh, M92, our value sits 0.09 Gyr above their quoted upper bound, comfortably within the combined uncertainty of the two analyses. Our ages run systematically older than the turn-off-and-horizontal-branch ages of VandenBerg et al. (2013) and Dotter et al. (2010), by a broadly similar margin across the sample, typically 1.0–1.5 Gyr.

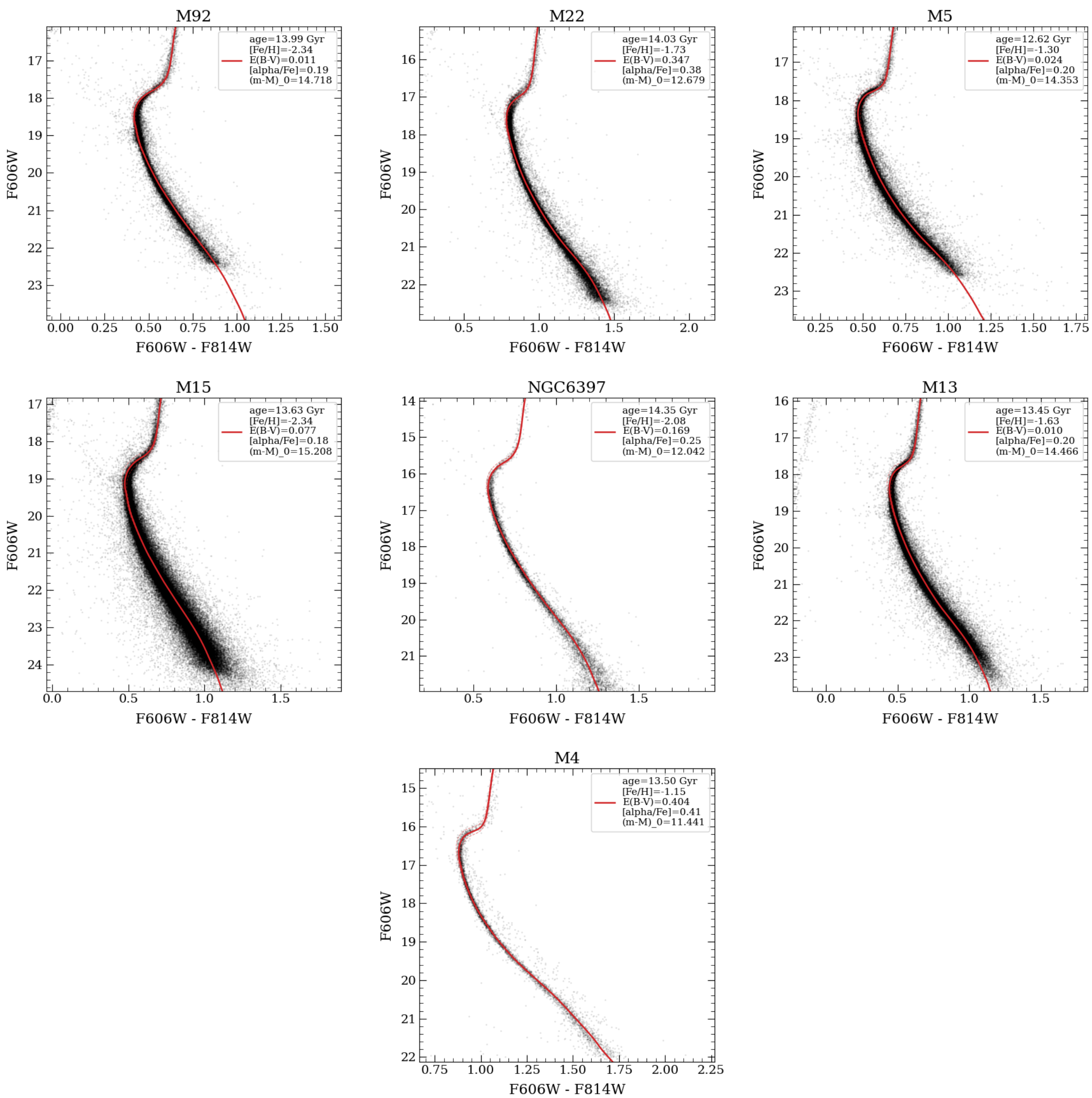

Figure 8: Best-fit DSED isochrone, solid coloured line, overlaid on the membership-selected, differential-reddening-corrected colour-magnitude diagram of each of the seven programme clusters, evaluated at the posterior median age, metallicity, distance modulus and reddening of each cluster.

3.2 Computation of the Friedmann Integral

The parameters entering the Friedmann integral, together with their sources, are summarised in Table 5. The derivation of Ω_Λ and Ω_r from these values is given in Section 2.2.7. Evaluating Equation (15) with these parameters, and propagating their uncertainties as described in Section 2.2.9, gives an age of the Universe of

$$t_0 = 13.792 \pm 0.111\, Gyr$$

in excellent agreement with the age tabulated directly by the Planck Collaboration for the identical parameter combination, 13.787 ± 0.020 Gyr, a difference of only 0.005 Gyr. We attribute this small residual difference to the rounding of the Planck table to four significant figures, and to our use of a simplified, massless treatment of the radiation component in place of the full Boltzmann-code treatment of the massive neutrino included in the Planck analysis. Both effects are far smaller than either quoted uncertainty.

Table 5: Cosmological parameters adopted in the Friedmann integral, with their source in Planck Collaboration et al. (2020).

Parameter	Value	Source
Ω_m	0.3111 ± 0.0056	Planck 2018 VI, Table 2, TT,TE,EE+lowE+lensing+BAO
Ω_Λ	0.6881	derived Closure relation, this work, Sect. 2.2.7
Ω_k	0.0007 ± 0.0019	Planck 2018 VI, eq. 47b, curvature extension, same data
Ω_r	9.14×10^{-5}	Derived, Fixsen 2009, Planck 2018 VI, fixed N_eff = 3.046
H_0	$67.66 \pm 0.42 kms^{-1}Mpc^{-1}$	Planck 2018 VI, Table 2, TT,TE,EE+lowE+lensing+BAO

4. DISCUSSION

The seven ages determined in Section 3.1 are compared with the literature in Table 4. Two comparisons are especially informative. Dotter et al. (2010), whose Table 2 supplies six of our seven priors, fit the same ACS Survey photometry with the same DSED stellar models used here, but match only the turn-off and horizontal-branch magnitudes rather than the full colour-magnitude diagram. Because the data, models and, for six of seven clusters, the literature-sourced priors are all held in common, this comparison isolates the effect of the fitting method itself. VandenBerg et al. (2013) provide a second, fully independent check, using their own stellar models and largely independent photometry.

Every one of our seven ages is older than the corresponding literature value in both comparisons, by a fairly consistent margin. The mean difference is 0.63 Gyr, with a range of 0.37–1.00 Gyr, relative to Dotter et al. (2010), and 1.37 Gyr, with a range of 0.88–2.00 Gyr, relative to VandenBerg et al. (2013). Given our combined statistical and systematic uncertainty of order 1-1.5 Gyr, most individual clusters remain consistent with both comparisons at the 1σ level. However, the offset runs in the same direction for every cluster rather than scattering above and below zero, indicating a systematic difference between the methods rather than chance. Since the Dotter et al. (2010) comparison holds the photometry, models and most priors fixed, and differs from our analysis only in fitting the turn-off and horizontal branch alone, we consider the fitting method itself the most likely origin of this offset. Information from the main sequence and subgiant branch, absent from a turn-off-only fit, evidently pulls the joint posterior toward somewhat older ages for this grid and likelihood. This is reinforced by our close agreement with Valcin et al. (2020), whose method we follow directly, within their own quoted uncertainty for six of our seven clusters.

Two clusters, NGC 6397 and M22, have posterior median ages that nominally exceed both the Friedmann-integral age of the Universe and the Planck value, but in both cases the excess, 0.56 Gyr and 0.24 Gyr respectively, is well within the combined uncertainty of the cluster age, and is not unique to our sample. Several of the 68 clusters analysed by Valcin et al. (2020) similarly exceed the Planck age without this being treated as evidence of tension, since some clusters scattering above an external reference value is expected behaviour for a sample of Bayesian posteriors of this size. M22's elevated age is plausibly connected to its well-documented multiple stellar populations and intrinsic abundance spread (Marino et al. 2011), which broaden the observed main sequence and subgiant branch beyond what is expected for a single-metallicity population and can bias a single-isochrone fit. M22 is, independently, the one cluster excluded from the Dotter et al. (2010) table for the same reason. Our fit does not model this structure explicitly, and we regard M22's elevated age as consistent with, rather than independent evidence for, this previously known property of the cluster. A similar pattern has been noted independently for M92 by Ying et al. (2023, 2025), whose age of 13.80 ± 0.75 Gyr agrees with our own to within 0.2 Gyr. This provides a useful cross-check that this is a property of the cluster rather than a pipeline artefact.

We find no evidence, across the seven clusters, of correlation between fitted age and fitted distance modulus, reddening or $[\alpha/Fe]$. The reddening prior of Section 2.1.4 is therefore not driving the age determination for any cluster, indicating that the age–distance–reddening degeneracy that limits turn-off-only analyses has, in practice, been broken by the additional information used here. The $[\alpha/Fe]$ posteriors, while individually weak, sit close to their literature priors in every case and disfavour values above roughly 0.6, in agreement with the corresponding finding of Valcin et al. (2020) for their much larger sample.

Because our pilot sample comprises seven clusters, against the 68 analysed by Valcin et al. (2020), we do not attempt to combine our individual posteriors into a population-level estimate of the age of the oldest globular clusters, nor to propagate this further into a globular-cluster-based estimate of the age of the Universe, as attempted with a substantially cruder methodology in an earlier version of this analysis. With a sample of this size the resulting distribution would be dominated by individual-cluster statistical uncertainty rather than any population property. We regard the present determination as a proof-of-concept validation of the method against an independent cosmological result, rather than a competitive, independent measurement of the age of the Universe in its own right. Extending the pilot sample toward the full Valcin et al. (2020) sample is a natural direction for future work, since the procedures of Section 2.1 are already general to any cluster in the ACS Survey.

Taken together, the two independent determinations presented here are mutually consistent. Every cluster age agrees, within its uncertainty, with the cosmological value, and none provides statistically significant evidence for an age of the Universe different from that derived from the Planck parameters. This consistency, between an age inferred from resolved stellar populations in the Milky Way and one inferred from the CMB power spectrum at a redshift of about 1100, is a non-trivial consistency-check of the Λ CDM model, since the two methods share essentially no common systematic uncertainty. An error in the DSED opacity tables, for example, would have no bearing on the Planck power-spectrum fit, and vice versa.

The persistent Hubble tension, Section 1.2.3, is not directly addressed by either determination presented here, since our cluster ages do not, in this pilot sample, constrain H_0 independently, and our Friedmann-integral calculation adopts the Planck H_0 by construction. We note, however, that adopting the locally measured value $H_0 = 74.03\ km\,s^{-1}\,Mpc^{-1}$ in place of the Planck value would reduce the Friedmann-integral age by roughly 1.5 Gyr, to a value that would sit in tension with several of our seven cluster ages at more than 1σ. This illustrates why any proposed resolution of the tension must ultimately be checked against the globular cluster age constraint, and not against the CMB power spectrum alone. Resolving it remains an important open problem, one to which larger-sample globular cluster age determinations of the kind attempted here may eventually contribute an independent constraint.

5. CONCLUSION

We have presented two independent determinations of the age of the Universe. From the colour-magnitude diagrams of seven Galactic globular clusters, fitted jointly for age, distance, reddening, metallicity and $[\alpha/Fe]$ under a Bayesian framework, we obtain ages of 12.62-14.35 Gyr, in agreement with previously published values for the same clusters. From the Friedmann integral, evaluated with the Planck 2018 cosmological parameters and with full propagation of their uncertainties, we obtain an age of the Universe of 13.792 $\pm$ 0.111 Gyr, in excellent agreement with the value quoted directly by the Planck Collaboration for the same parameter combination. Every cluster age determined in this work is consistent, within its uncertainty, with this cosmological value. Extending the present pilot sample to the full set of clusters analysed by Valcin et al. (2020) would allow a population-level, globular-cluster-based estimate of the age of the Universe to be obtained with the pipeline presented here, and is a natural direction for future work.

6. ACKNOWLEDGEMENTS

I would like to thank the teams behind the Hubble Space Telescope ACS Survey of Galactic Globular Clusters and the Hubble Space Telescope UV Legacy Survey of Galactic Globular Clusters for making the photometric and proper-motion catalogues used in this analysis publicly available. I also acknowledge the Dartmouth Stellar Evolution Database for providing the stellar evolution models used throughout the globular cluster age analysis, and the developers of the Python scientific computing tools used for the numerical calculations and Bayesian inference. Finally, I thank the Planck Collaboration for making the 2018 cosmological parameter results publicly available.

7. REFERENCES

Anderson, J., Sarajedini, A., Bedin, L. R., et al. 2008, The Astronomical Journal, 135, 2055

Baumgardt, H., & Vasiliev, E. 2021, Monthly Notices of the Royal Astronomical Society, 505, 5957, https://arxiv.org/pdf/2105.09526.pdf

Bedin, L. R., Cassisi, S., Castelli, F., et al. 2005, Monthly Notices of the Royal Astronomical Society, 357, 1038

Bellini, A., Anderson, J., Bedin, L. R., et al. 2017, The Astrophysical Journal, 842, 6

Bussey, P. J. 2017, Contemporary Physics, 58, 381

Chaboyer, B. 1995, The Astrophysical Journal, 444

Dotter, A., Chaboyer, B., Jevremović, D., et al. 2008, The Astrophysical Journal Supplement Series, 178, 89, https://arxiv.org/pdf/0804.4473.pdf

Dotter, A., Sarajedini, A., Anderson, J., et al. 2009, The Astrophysical Journal, 708, 698

Fixsen, D. J. 2009, The Astrophysical Journal, 707, 916

Foreman-Mackey, D., Hogg, D. W., Lang, D., & Goodman, J. 2013, Publications of the Astronomical Society of the Pacific, 125, 306, https://arxiv.org/pdf/1202.3665.pdf

Goswami, G. K. 2019, Canadian Journal of Physics, 97, 588

Harris, W. E. 1996, The Astronomical Journal, 112, 1487

Ikape, M. 2024, Scholaris.ca, https://utoronto.scholaris.ca/items/70582efd-289c-41b5-8015-784e493eb4c2

K. Brogaard, VandenBerg, D. A., Bedin, L. R., et al. 2017, Monthly Notices of the Royal Astronomical Society, 468, 645, https://academic.oup.com/mnras/article/468/1/645/2993894

Krauss, L. M. 2003, Science, 299, 65, https://www.astro.caltech.edu/~george/ay127/readings/KraussChaboyer2003.pdf

Legnardi, M. V., Milone, A. P., Cordoni, G., et al. 2023, Monthly Notices of the Royal Astronomical Society, 522, 367

Libralato, M., Bellini, A., Piotto, G., et al. 2019, The Astrophysical Journal, 873, 109

Libretexts. 2019, Physics LibreTexts (Libretexts), https://phys.libretexts.org/Courses/University_of_California_Davis/Physics_156%3A_A_Cosmology_Workbook/01%3A_Workbook/1.27%3A_Cosmic_Microwave_Background_Anisotropies

Marino, A. F., Villanova, S., Milone, A. P., et al. 2011, The Astrophysical Journal, 730

Milone, A. P., Piotto, G., Bedin, L. R., et al. 2012, Astronomy & Astrophysics, 540

Neeley, J. R., Marengo, M., Bono, G., et al. 2015, The Astrophysical Journal, 808, 11

Nemiroff, R. J., & Patla, B. 2008, American Journal of Physics, 76, 265

Peters, T. 2013, Contemporary Physics, 54, 307

Planck Collaboration. 2020, Astronomy & Astrophysics, 641

Pritzl, B. J., Venn, K. A., & Irwin, M. 2005, The Astronomical Journal, 130, 2140
Riess, A. G., Casertano, S., Yuan, W., Macri, L. M., & Scolnic, D. 2019, ApJ, 876, 85, https://ui.adsabs.harvard.edu/abs/2019ApJ...876...85R/exportcitation
Rowan, L., & Coontz, R. 2003, Science, 299, 59
Sarajedini, A., Bedin, L. R., Chaboyer, B., et al. 2007, The Astronomical Journal, 133, 1658
Sirianni, M., Jee, M. J., Benítez, N., et al. 2005, Publications of the Astronomical Society of the Pacific, 117, 1049
Uzan, J.-P., & Lehoucq, R. 2001, European Journal of Physics, 22, 371
Valcin, D., Bernal, J. L., Jimenez, R., Verde, L., & Wandelt, B. D. 2020, Journal of Cosmology and Astroparticle Physics, 2020, 002, https://arxiv.org/pdf/2007.06594.pdf
VandenBerg, D. A., Brogaard, K., Leaman, R., & Casagrande, L. 2013, The Astrophysical Journal, 775, 134, https://arxiv.org/pdf/1308.2257.pdf
Verde, L., Treu, T., & Riess, A. G. 2019, Nature Astronomy, 3, 891, https://arxiv.org/pdf/1907.10625.pdf
Wagner-Kaiser, R., Sarajedini, A., von Hippel, T., et al. 2017, Monthly Notices of the Royal Astronomical Society, 468, 1038
Ying, J. M., Chaboyer, B., Boudreaux, E. M., et al. 2023a, The Astronomical Journal, 166, 18, https://arxiv.org/abs/2306.02180
Ying, J. M., Chaboyer, B., Boudreaux, E. M., et al. 2023b, The Astronomical Journal, 166, 18, https://arxiv.org/abs/2306.02180
Ying, J. M., Chaboyer, B., & Du, W. 2024, The Astrophysical Journal, 970, 184